

Artificial Intelligence-Assisted Bioinformatics, Microneedle, and Diabetic Wound Healing: A “New Deal” of an Old Drug

Yanan Xue,[▽] Cheng Chen,[▽] Rong Tan, Jingyu Zhang, Qin Fang, Rui Jin, Xiangyu Mi, Danying Sun, Yinan Xue, Yue Wang, Rong Xiong, Haojian Lu,* and Weiqiang Tan*



Cite This: *ACS Appl. Mater. Interfaces* 2022, 14, 37396–37409



Read Online

ACCESS |



Metrics & More



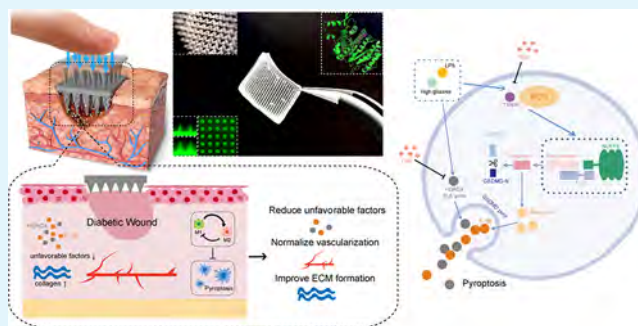
Article Recommendations



Supporting Information

ABSTRACT: Diabetic wounds severely influence life, facing grand challenges in clinical treatments. The demand for better treatment is growing dramatically. Diabetic wound healing is challenging because of inflammation, angiogenesis disruptions, and tissue remodeling. Based on sequencing results of diabetic patients' skins and artificial intelligence (AI)-assisted bioinformatics, we excavate a potential therapeutic agent Trichostatin A (TSA) and a potential target histone deacetylase 4 (HDAC4) for diabetic wound healing. The molecular docking simulation reveals the favorable interaction between TSA and HDAC4. Taking advantage of the microneedle (MN) minimally invasive way to pierce the skin barrier for drug administration, we develop a swelling modified MN-mediated patch loaded with TSA to reduce the probability of injection-caused iatrogenic secondary damage. The MN-mediated TSA patch has been demonstrated to reduce inflammation, promote tissue regeneration, and inhibit HDAC4, which provides superior results in diabetic wound healing. We envisage that our explored specific drug TSA and the related MN-mediated drug delivery system can provide an innovative approach for diabetic wound treatment with simple, effective, and safe features and find a broad spectrum of applications in related biomedical fields.

KEYWORDS: artificial intelligence, bioinformatics, Trichostatin A, microneedle, diabetic wounds



1. INTRODUCTION

Diabetes wounds, especially diabetic foot ulcers, occur in 30% of diabetic patients, which causes significant morbidity and mortality.¹ Unlike normal cutaneous wounds, the prolonged inflammatory response of diabetic damage results in poor wound healing.² Under conventional wound dressing treatment, the traditional diabetic wound treatment effect is insufficient, exacerbates, and leads to amputation.³ The normal healing process is severely interfered with in such chronic wounds and disorders. Eventually, it causes persistent inflammation and dysfunctional tissue remodeling, leading to a hard time to heal the wound and increasing the risk of infection.⁴ Thus, the demand for better wound treatments is growing dramatically.⁵

Inflammation modulation is one of the most compelling and effective ways to promote diabetic chronic wound healing.⁶ Pyroptosis is a type of inflammatory cell death that relies on the NLRP3 inflammasome-mediated cleavage of gasdermin D (GSDMD) followed by the creation of pores on plasma membranes through which interleukin-1 β (IL-1 β) is released.⁷ There is a well-known sensor molecule known as NLRP3 inflammasome that connects diabetic metabolism with inflammation,^{8,9} which will increase the risk of immune cell pyroptosis and exacerbate the wound severity.¹⁰ The

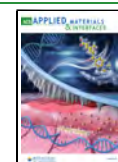
imbalance between pro-inflammatory (M1) and anti-inflammatory (M2) macrophage phenotypes also hampers wound healing.¹¹ In diabetic wounds, the M1 phenotype macrophage releases pro-inflammatory cytokines, such as tumor necrosis factor alpha (TNF- α) and interleukin 6 (IL-6), which inhibit collagen synthesis and stimulate apoptosis of cells. On the other hand, M2 macrophages can regulate anti-inflammatory reactions, encourage fibroblast proliferation, maintain angiogenesis, and rebuild the extracellular matrix (ECM).¹²

Insulin is a common glucose-lowering drug widely utilized in diabetic therapy through subcutaneous infusion. However, in the chronic wound bed, uncontrolled pro-inflammatory cytokine increases peripheral insulin resistance.¹³ Long-term use of insulin can be associated with hypoglycemia¹⁴ and may trigger the development of lipodystrophy, which is not conducive to wound healing.^{15,16} Therefore, a specific medicine for effective diabetic wound healing is in great demand for

Received: May 24, 2022

Accepted: July 22, 2022

Published: August 1, 2022



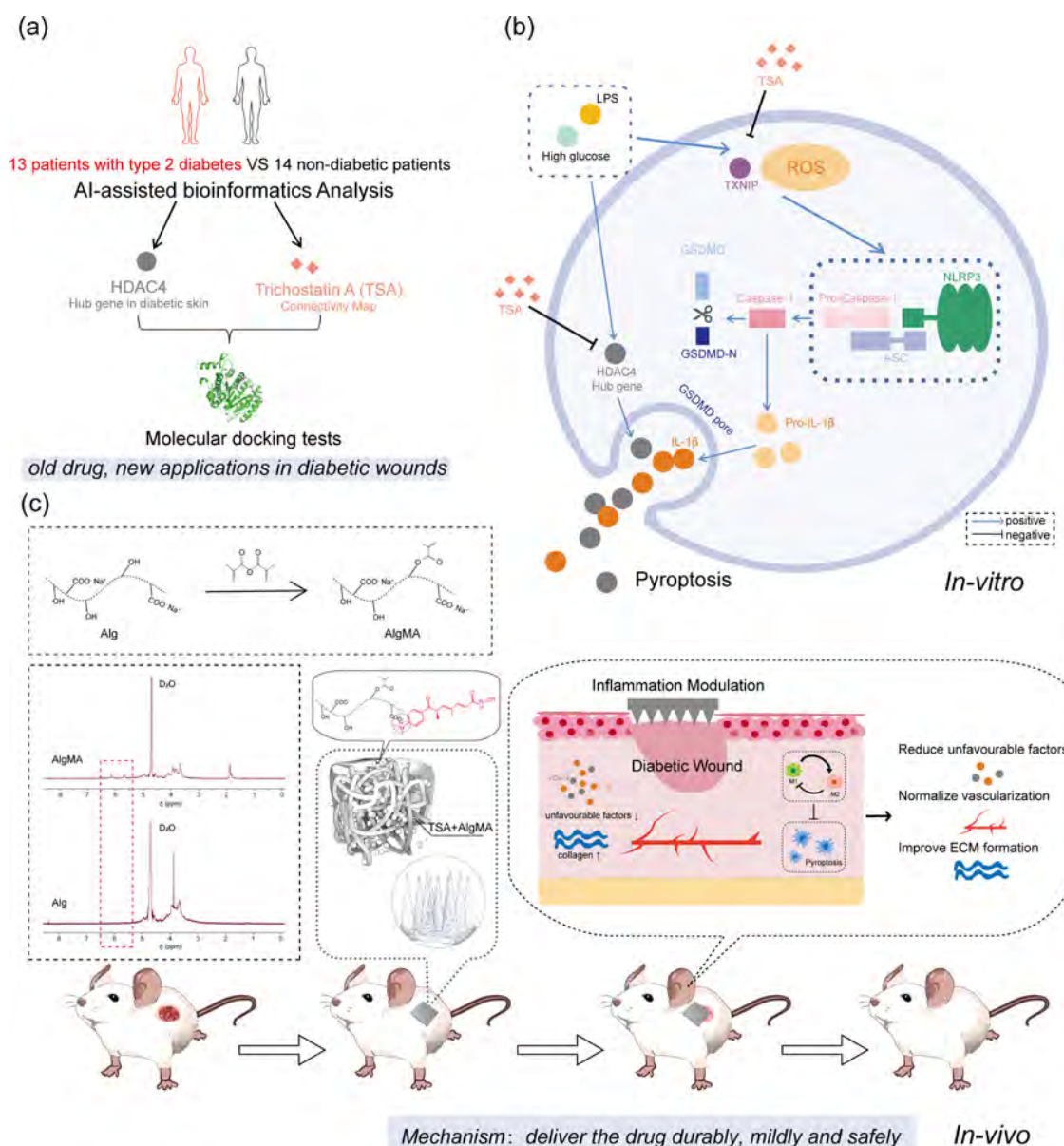


Figure 1. Schematic illustration of research ideas in this study. (a) Thirteen patients with type 2 diabetes and 14 non-diabetic patients' skin sequencing data are obtained from the GEO datasets. The therapeutic potential of TSA and hub gene HDAC4 in diabetic wounds is excavated through the AI-assisted bioinformatics analysis. (b) TSA regulation pyroptosis and HDAC4 in vitro. (c) Characterization of the MN-mediated TSA patch, consisting of a TSA-loaded AlgMA microneedle array for the treatment of dressings in the chronic wounds: AlgMA is a modified sodium alginate added double bond, and the proton nuclear magnetic resonance (PMR) shows successful conjugation. In this study, TSA and AlgMA are bound together through electrostatic interactions. Schematic illustration of using the MN-mediated TSA patch to treat diabetic wounds in vitro with various therapeutic avenues: reduce unfavorable factors such as inflammatory factors, diabetic hub genes; normalize vascularization; improve ECM formation.

emerging application in clinical diabetic wound therapies.¹⁶ The connectivity map (Cmap) dataset reveals the genome-wide gene expression data of drug and disease connection through AI-assisted bioinformatics, which is available for new deals of old medicines and new drug mining, reducing the drug development research resources and cost.¹⁷ Some researchers use Cmap to empower new deals of old drugs, such as disulfiram for diabetic angiopathy (DA)¹⁸ and atractyloside for type 2 diabetes.¹⁹ However, there is little research on diabetic wounds based on this dataset. Through the various AI-assisted bioinformatics approaches, including GSE144441, Cmap dataset, and molecular docking test, the therapeutic potential of TSA and hub gene HDAC4 in diabetic wounds is excavated.

Typified by the histone deacetylase (HDAC) family, acetylation and deacetylation are common protein modifications in epigenetic regulation. The HADC family plays a significant role in diabetic wounds or inflammation regulation,²⁰ e.g., HDAC6 regulates IL-1 β secretion and IL-10 expression in diabetic wounds' macrophages,²¹ targeting HDAC6 weakens macrophage pyroptosis via the NF- κ B/NLRP3 pathway,²² and HDAC3 negatively regulates the M2 macrophage phenotype.²³ Moreover, a recent study finds that HDAC11 can aggravate the endothelial cell pyroptosis through NLRP3 inflammasome,²⁴ which provides reference and enlightenment for diabetic wounds related to cell pyroptosis

and angiogenesis. However, it is still unknown if HDAC4 could play a role in diabetic wounds (Figure 1a).

The MN-mediated patches with various matters have been developed for wound treatment, such as black phosphorus,²⁵ magnesium,²⁶ porous metal–organic framework (MOF),²⁷ and exosome.²⁸ Of existing drug delivery systems,²⁹ a painless and easy-to-use transdermal MN patch is an attractive option for a minimally invasive way to pierce the skin barrier for drug administration.³⁰ MN patches offer a robust matrix with high drug loading potential. The integrated design of penetration and medication is a superior candidate for wound healing and can avoid injection-caused iatrogenic secondary trauma.³¹

Under the guidance of artificial intelligence (AI)-assisted bioinformatics, this study demonstrates an MN-mediated patch that simultaneously regulates inflammation, tissue regeneration, and hub gene for diabetic wound treatment. The embedded drug TSA, once used in anti-tumor³² and non-diabetic skin repair,³³ demonstrates its therapeutic capacity in wounds. However, it has not been used for diabetic wounds, which tend to have severe inflammation, difficult tissue remodeling, and insufficient blood supplement. The MN-mediated patch is fabricated via swelling modified sodium methacrylate-alginate (AlgMA), which can penetrate the wound under a dry state and release the drug consistently and controllably after transitioning into a polyporous hydrogel.³⁴ Through in vitro and in vivo experiments and relative bioinformatics analysis, the loaded TSA drug demonstrates its capacity to inhibit NLRP3 inflammasome activation, decrease the risk of NLRP3-mediated macrophage pyroptosis, and promote macrophage phenotype polarization. Meanwhile, our proposed MN-mediated TSA patch can also inhibit the diabetic wounds' target gene and hub gene HDAC4, indicating another pathway in diabetic wound regulation (Figure 1b,c). Moreover, based on the designed MN-mediated patch treatment, the regeneration of blood vessels and collagen fibers is promoted well. Our proposed method implements simultaneous inflammation, tissue regeneration, and hub gene regulation for diabetic wound treatment in a low invasive and drug-controlled release mode, which could greatly benefit diabetic wound healing and related biomedical fields.

2. EXPERIMENTAL SECTION

2.1. Diabetes Skin Data and Genetic Analysis. The GSE144441 (type 2 diabetes patients' skin genes) dataset was downloaded from the GEO database³⁵ for free. Through GO analysis and KEGG pathway enrichment analysis drawn by Meatscape,³⁶ DEGs of GSE144441 reveal the predominant association with epigenetic regulation, immunology, angiogenesis, and tissue remodeling. In the DEG regulation network drawn by STRING,³⁷ 10 genes (HDAC4, SOD2, ACTB, VWF, ITGAV, ITGA3, ITGA9, LAMB1, UBQLN1, and ATAD2B) were selected as hub genes due to CytoHubba³⁸ from Cytospace (version 3.7.2).³⁹ Among the top 10 agents, TSA is the top 1 agent. Notably, AutoDock Vina⁴⁰ molecular docking tests show that TSA can interact well with HDAC4 (PDB code: 2VQM).

2.2. Animals, Cells, and Materials. Zhejiang University's Animal Care and Use Committee authorized all animals. At the Zhejiang Academy of Medical Sciences, Sprague–Dawley (SD) rats (male, 8 weeks old) were obtained. Rats were kept in a home with a regular light–dark cycle, a constant temperature of 21–23 °C, a humidity of 45–50%, and access to enough food and water. After 1 week of adaptive feeding, SD rats got a single intraperitoneal injection of streptozotocin (65 mg kg⁻¹) in 0.1 M citrate buffer (pH 4.5). One week after the last injection, diabetic rats were selected from those whose fasting random blood glucose levels exceed 16.7 mmol L⁻¹.

Tables S3 and S4 (Supporting Information) show the blood glucose fluctuations and body weights of diabetic and control rats. In brief, diabetic rats were anesthetized with the aid of isoflurane (oxygen delivered at 3–4 L min⁻¹ with 4% isoflurane for induction and 2% isoflurane for maintenance) and sterilized with 5% povidone-iodine. Microscissors were used to create symmetrical full-thickness excisional wounds measuring 10 mm in diameter. RAW264.7 cell and ECFCs were obtained from Procell (Wuhan, China), AlgMA and lithium phenyl-2,4,6-trimethyl-benzoyl phosphinate (LAP) were acquired from EFL (Suzhou, China), Trichostatin A (TSA) was purchased from MCE (New Jersey, USA), and fluorescein isothiocyanate labeled bovine serum albumin (FITC-TSA) was purchased from Ruixibio (Xian, China).

2.3. Characterization. In this study, the optical and fluorescence images of the MN-mediated TSA patch were captured using microscopy (Dino-Lite AM73915MZTL) and a microscope (NIKON Ci-L) geared up with CI-FL-2 Epi-Fluorescence attachment, respectively. SEM pictures were taken through two scanning electron microscopes (Hitachi S-3700; Hitachi SU-70). The mechanical strength of MN-mediated patches with different AlgMA concentrations was tested by an electronic universal testing machine (WH-70).

2.4. Evaluation Cytocompatibility of the Hydrogels. A live/dead assay was used to evaluate the cytotoxicity of the hydrogels. On the bottom of the 24-well plate, 30 L hydrogels were cross-linked by UV light under aseptic conditions. Next, 1.5×10^4 ECFCs were seeded per well on the gel. The hydrogels were incubated with a live/dead detection kit in accordance with the procedure after being cultured for 1, 3, and 5 days. With the use of an inverted microscope, the cells were viewed.

2.5. Assessment of Cell Proliferation. Cell proliferation was detected using a Cell Counting Kit-8 (CCK-8) (APExBIO, USA). On the bottom of a 96-well plate, cross-linking took place using 10 μ L of gel each well. The plate was then cultivated with 5000 cells per well at this point. According to the kit's instructions, 10 μ L of CCK-8 was added on days 1, 3, and 5. A microplate reader measured the absorbance at 450 nm after incubation. The cell proliferation = $(As - Ab)/(Ac - Ab)$. As is representative of the test group, Ab stands for the blank group, and Ac represents the control group.

2.6. Cell Migration Assessment by Gap Closure. The gap closure experiment was carried out to investigate the impact of hydrogel on ECFC migration. ECFCs (1×10^3 cells per well) were cultured in 8% AlgMA hydrogels, and 8% AlgMA containing TSA coated the 24-well plate with a hydrogel plug in the middle (Cat# CBA-125; Cell Biolabs) for 24 h. Meanwhile, one group was established as the TSA treatment group without the AlgMA hydrogel. After that, the plug was taken out to make a space or gap without cells. Under a microscope (NIKON Ci-L), the number of cells moving into the middle gap was counted.

2.7. Cell Adhesion Assessment. First, UV light was used to cross-link 30 μ L of hydrogel each well in a 24-well plate under aseptic conditions. Next, 2.5×10^5 ECFCs per well were seeded on the gel and cultured for 4 h. Meanwhile, the same number of ECFCs was seeded on the 24-well TCP cell culture dish to establish the control group. After 4 h, the medium was removed and PBS was used to rinse ECFCs three times gently. Finally, cells were stained with a DAPI dye for 5 min and were observed under a microscope (NIKON Ci-L).

2.8. Quantitative Real-Time PCR. An RNA extraction kit (Biyuntian, Shanghai, China) was used to extract the total RNA from cells. Complementary DNA was synthesized from the reverse transcription package AG11706 (Accurate Biotechnology, Hunan, China). The qRT-PCR was carried out by the SYBR-Green system (Solarbio, Beijing, China) and Q2000A real-time PCR system (LongGene, Hangzhou, China). The outcomes were normalized to the expression levels of GAPDH by the $2^{-\Delta\Delta C_t}$ approach for quantification. All primers used are listed in Table S2 (Supporting Information).

2.9. Wound Healing Study. On the back of anesthetized rats, 1 cm in diameter, spherical skin pores were resected to produce a wound. Then, these rats were divided into five groups (each group has

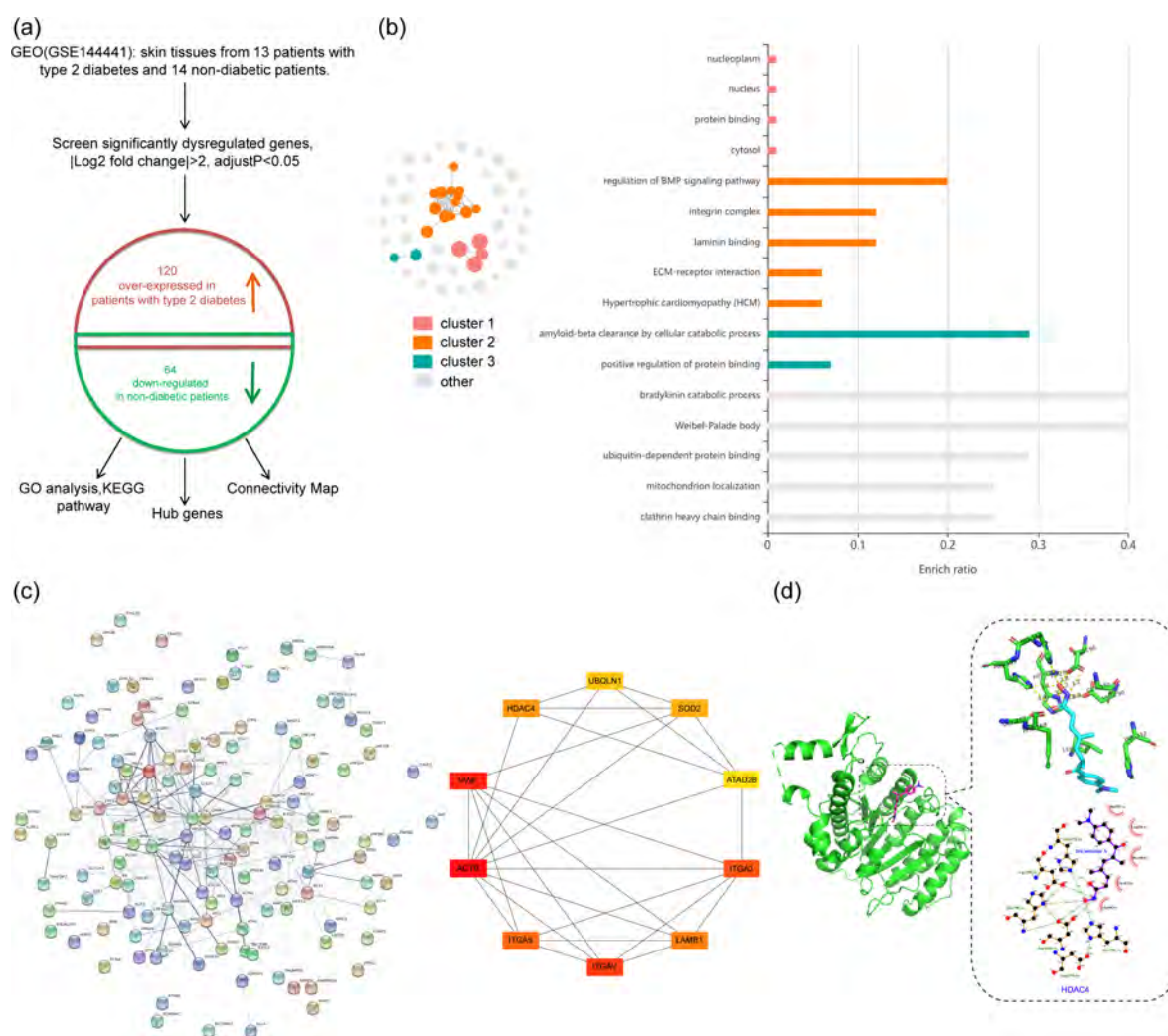


Figure 2. Schematic illustration of AI-assisted bioinformatics analysis. (a) GSE14441 data, including 13 patients with type 2 diabetes and 14 non-diabetic patients. After screening the differently expressed genes (DEGs) with log 2 fold change >2, adjust $P < 0.05$, 120 genes upregulated and 64 genes downregulated. Next, we perform a more comprehensive AI-assisted bioinformatics analysis, including GO analysis, KEGG pathway, hub genes, and connectivity map, according to the DEGs. (b) The GO and KEGG pathway analyses include gene regulation, immunology, and tissue remodeling. The enriched terms visualized in cirFunMap on the left (each node represents an enriched phrase, and the color of the node denotes a different cluster. The node size denotes six levels of enrichment, ranging from small to large: $[0.05, 1]$, $[0.01, 0.05]$, $[0.001, 0.01]$, $[1 \times 10^{-10}, 0.0001]$, and $[0, 1 \times 10^{-10}]$). On the right, a bar plot shows the enhanced terms. The color of the bar correlates to the color of the circular network in cirFunMap, which denotes unique clusters, and the length of the bar shows the enrich ratio determined as each row represents an enriched function. The top five terms with the highest enrichment ratio for each cluster, if there are more than five terms in a cluster, will be shown). (c) Networks (PPI) of DEGs obtained from STRING are on the left. On the right, 10 genes (HDAC4, SOD2, ACTB, VWF, ITGAV, ITGA3, ITGA9, LAMB1, UBQLN1, and ATAD2B) are selected as hub genes due to Cytohubba from Cytospace (version 3.7.2). Among these 10 hub genes, seven are significantly downregulated (SOD2, ACTB, VWF, ITGA3, ITGA9, UBQLN1, and ATAD2B) while three are highly upregulated (HDAC4, ITGAV, and LAMB1). (d) The docking affinities (kcal mol⁻¹) of HDAC4 are -9.1 . These results suggest that TSA can interact effectively with HDAC4.

six rats), the MN-mediated TSA patch (1.5 mg of TSA per patch on days 0, 3, and 6; 4.5 mg of TSA per rat with 9 days), MN-mediated patch without TSA (treatment similar with the MN-mediated TSA patch), TSA injection (7.5 mg mL⁻¹ TSA in DMSO, twice a week, 0.2 mL solution including 1.5 mg of TSA, per injection on days 0, 3, and 6; 4.5 mg of TSA per rat with 9 days), DMSO injection (injection similar with TSA injection), and DM control (non-treatment). As TSA is the first application in the diabetic wound model, the dose administered (single dose of 5 mg/kg) is based on a previous study about the breast cancer model.³² Finally, rats were returned to cages with food and water. The wounds were photographed and measured using ImageJ software on days 0, 3, 5, 7, and 9 following the procedure. The percentage of healed area = $[W(3, 5, 7, 9)/W_0] \times 100\%$, where W_0 and $W(3, 5, 7, 9)$ represent healed areas on days 0 and 3, 5, 7, and 9.

2.10. Western Blotting Analysis and ELISA. First, fresh tissues and cells were homogenized in the RIPA buffer MA0151 (Meilunbio, Dalian, China) combined with a protease inhibitor cocktail MB2678 (Meilunbio, Dalian, China). Next, the supernatant protein suspension was obtained by centrifugation. Protein concentrations were identified by a BCA protein assay kit (Servicebio, Wuhan, China) and protein nucleic acid analyzer Nano-800 (Jiapeng Instruments, Shanghai, China) and then separated on FuturePAGE (ACE, Nanjing, China). The proteins were transferred to a PVDF membrane (EpiZyme, Shanghai, China) and incubated overnight before being blocked for 1 h with 5% nonfat milk. The membranes were added with the primary antibodies overnight at 4 °C. Table S5 of the Supporting Information includes a list of the principal antibodies that were utilized. The next day, the membranes were incubated with a 1:3000 dilution of an HRP-conjugated anti-mouse or anti-rabbit secondary antibody

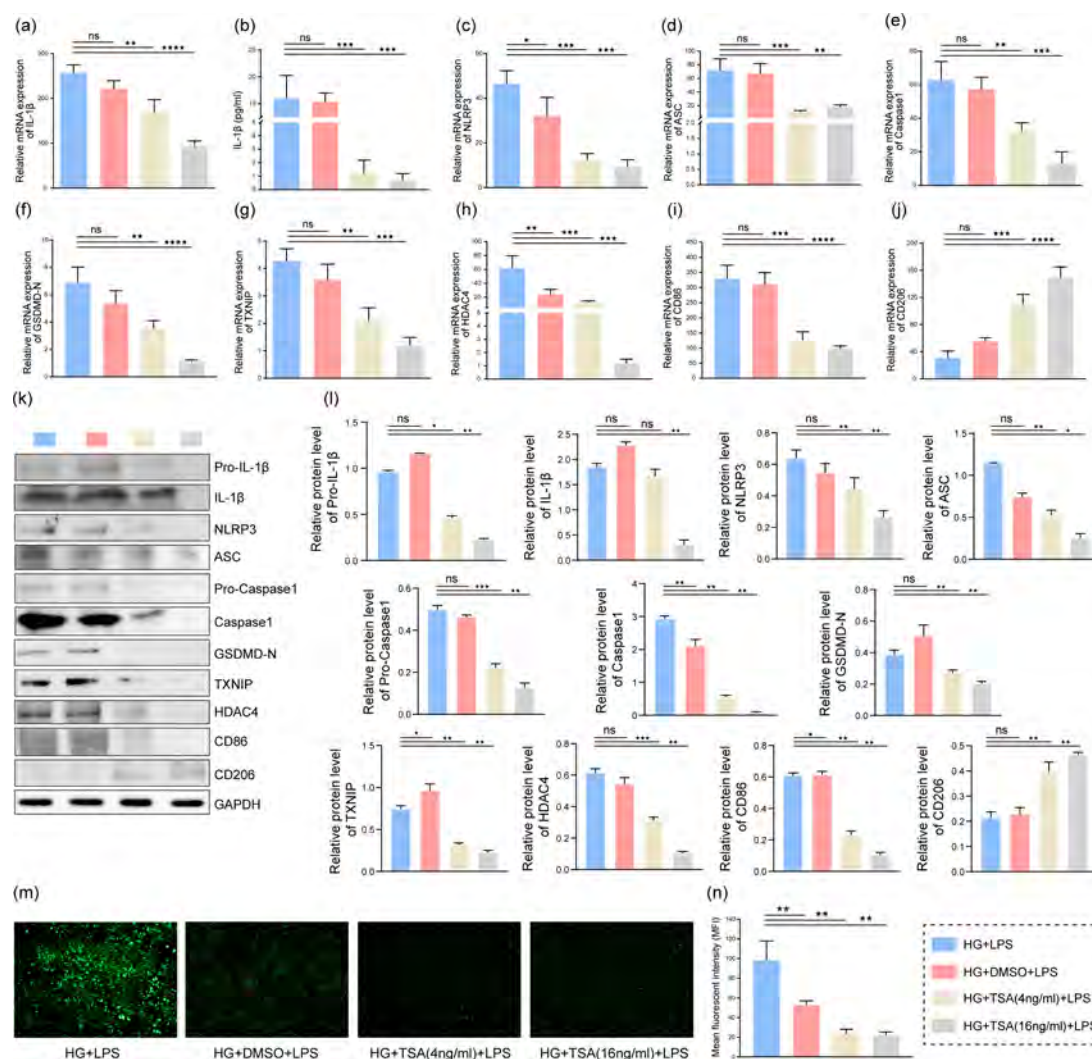


Figure 3. Evaluation of TSA in vitro. Relative gene expressions and protein expressions of pyroptosis direct related genes, including IL-1 β , NLRP3, ASC, Caspase1, and GSDMD-N (a–f, k, l). Relative gene and protein expressions of pyroptosis indirect related gene TXNIP and diabetic wound hub gene HDAC4 (g, h, k, l). Relative gene and protein expressions of M1 macrophages marker and M2 macrophages marker (i, j, k, l). ROS expression (m) and mean gray value of ROS (n) in a different group, which is downregulated in TSA groups, compared to the HG + LPS group. This indicates the successful ROS regulation of our explored drug TSA. Data are represented as mean \pm SD ($N = 3$, each experiment is performed thrice). * $P < 0.05$, ** $P < 0.01$, *** $P < 0.001$, **** $P < 0.0001$.

(ProteinTech, Wuhan, China) at room temperature for 30 min. The membranes were then washed in depth with TPBS three times. Finally, signals were detected by employing chemiluminescence with an ECL kit (Servicebio, Wuhan, China) and chemiluminescence imager JP-K600 (Jiapeng Instruments, Shanghai, China). ELISA was performed to assess inflammatory factor expression in RAW264.7 cells. A mouse TNF- α ELISA kit (cat. no.KE10002), mouse IL-1 β ELISA kit (cat. no.KE10003), and mouse IL-6 ELISA kit (cat.no.KE10007) were purchased from Proteintech (Wuhan, China).

2.11. Statistical Analysis. All statistical analyses were performed using the software packages R (version 3.6.2), GraphPad Prism (version 8), and Origin (version 9.1). All results were presented as means \pm SD. Statistical analysis was performed using the two-tailed Student's t -test and analysis of variance (ANOVA). The differences between experimental and control groups are considered statistically significant at $P < 0.05$.

3. RESULTS AND DISCUSSION

3.1. AI-Assisted Bioinformatics. Differently expressed genes (DEGs) of GSE144441 include 13 patients with type 2 diabetes and 14 non-diabetic patients. After screening the

DEGs with log 2 fold change > 2 and adjust $P < 0.05$, 120 genes upregulated and 64 genes downregulated. Next, we perform more comprehensive AI-assisted bioinformatics analysis, including the Gene Ontology (GO) analysis, the Kyoto Encyclopedia of Genes and Genomes (KEGG) pathway enrichment analysis, hub genes, and connectivity map (Figure 2a). The GO analysis and KEGG pathway enrichment analysis results are obtained from the KOBAS-i (KOBAS 3.0, KOBAS intelligent version)⁴¹ using a new machine learning-based method, Gene set analysis incorporating Prioritization and Sensitivity (CGPS).⁴² The significant enrichment terms of GO analysis and the KEGG pathway are displayed, including gene regulation, immunology, and tissue remodeling, for example, ECM-receptor interaction, regulation of the BMP signaling pathway, positive regulation of protein binding, and so on (Figure 2b and Figure S1). These enrichment terms guide therapeutic mechanisms in the direction of inflammation and tissue remodeling. The protein–protein interaction networks (PPI) of DEGs are obtained from STRING (<https://string-db.org/>), and 10 genes (HDAC4, SOD2, ACTB, VWF, ITGAV,

ITGA3, ITGA9, LAMB1, UBQLN1, and ATAD2B) are selected as hub genes due to Cytoscape with the maximal clique centrality algorithm (a kind of network topology algorithm)³⁸ from the Cytoscape (version 3.7.2). Among these 10 hub genes, three genes (HDAC4, ITGAV, and LAMB1) are highly upregulated, whereas seven genes (SOD2, ACTB, VWF, ITGA3, ITGA9, and ATAD2B) are strongly downregulated. Meanwhile, HDAC4 has a differential expression with log 2 fold change = 5.27, suggesting its target potential in treating diabetic chronic wounds (Figure 2c). Several types of medications with substantial scores are nominated based on the Cmap dataset prediction (Table S1). Among these, TSA ranks first and its modulation ability of myeloid progenitor plasticity and behavior in inflammation and the close correlation with the cell cycle have been reported.⁴³ Interestingly, the molecular docking studies further show that TSA can interact well with HDAC4, and the docking affinity (kcal mol⁻¹) of HDAC4 is -9.1 (Figure 2d). Above all, the AI-assisted bioinformatics guidance provides us with a brand new research perspective and has tremendous potential for promoting wound healing treatments.

3.2. Evaluation of TSA In Vitro. For macrophage in vitro experiments, the culture solution is deployed with the combination of high glucose (HG) (Figure S2a) and lipopolysaccharide (LPS) to simulate the cellular pyroptosis of diabetic wounds and screened for a suitable concentration of TSA.⁴⁴ Through qRT-PCR, as illustrated in Figure S2b–d, inflammatory cytokines IL-1 β , TNF- α , and IL-6 mRNA expressions are upregulated in macrophages stimulated by 35 mM glucose concentration. Thus, the subsequent experiments chose 35 mM HG as one of the pyroptosis conditions. With 35 mM HG and 1 μ g mL⁻¹ LPS stimulation, the concentrations of TSA are adopted as 4 and 16 ng mL⁻¹ for mimicking the medium and high stimulation concentrations, respectively (Figure S2e). As shown in Figure 3a, the group pre-cultured TSA with a concentration of 4 or 16 ng mL⁻¹ for an hour, and the secretion of IL-1 β is significantly inhibited. Moreover, the expression of IL-1 β released in the supernatant is significantly downregulated, compared to the pyroptosis group (HG + LPS) measured by enzyme-linked immunosorbent assay (ELISA) (Figure 3b). Further, protein analysis of the cell lysates also shows the downregulated expression of pro-inflammatory interleukin-1 β (Pro-IL-1 β) and IL-1 β in TSA treated macrophages, indicating the successful regulation of IL-1 β of our explored drug TSA (Figure 3k,l).

According to a previous study, HG and LPS stimulation of macrophages activate the NLRP3 inflammatory complex, which recruits ASC and Pro-Caspase-1, and then assembles into an activated NLRP3 inflammatory together.⁸ The NLRP3 inflammatory complex catalyzes the self-excision of Pro-Caspase1 into active Caspase1, an inflammatory caspase involved in both the maturation and secretion of Pro-IL-1 β through plasma membrane pores. GSDMD-N translocates to the plasma membrane, where it assembles to form pores through which IL-1 β is secreted from the cell.⁴⁵ To clarify whether TSA acts through the NLRP3 inflammatory complex and GSDMD-N to reduce IL-1 β , we examine the effect of TSA intervention on the expression and activation of the NLRP3-ASC-Caspase1 inflammatory complex and GSDMD-N in macrophages activated by LPS and high glucose. With the cooperation of HG and LPS, the mRNA expressions of NLRP3, ASC, Caspase1, and GSDMD-N are significantly elevated. With the TSA pre-treating for an hour, the secretion

of NLRP3, ASC, Caspase1, and GSDMD-N is inhibited significantly (Figure 3c–f). Moreover, the protein level results also reveal that the administration of TSA interventions has a significant impact on the downregulation of NLRP3, ASC, Caspase1 (including Pro-Caspase1), and GSDMD-N (Figure 3k,l).

It is suggested that increased intracellular reactive oxygen species (ROS) might be a pathway for activating the NLRP3 inflammatory complex and cell pyroptosis.⁴⁶ The ROS level of RAW264.7 cells is significantly upregulated in the HG + LPS group but dramatically reduced after TSA intervention, as shown in Figure 3m,n, indicating that TSA effectively inhibits intracellular ROS. Apart from ROS, thioredoxin interaction protein (TXNIP) may also directly induce the assembly and activation of the NLRP3 inflammatory complex. A previous study has reported that TXNIP can act as a binding factor to NLRP3, and their combination is essential for downstream inflammasome activation.⁴⁷ The HADC family plays a significant role in diabetic wounds or inflammation regulation, and the above research indicates that HDAC4 is the hub gene in diabetic wounds, but there are few reports about cellular pyroptosis in diabetic wounds. The mRNA and protein levels of TXNIP and HDAC4 in macrophages are examined for relation evaluation between the TXNIP, HDAC4, NLRP3 inflammatory complex, and cellular pyroptosis of diabetic wounds. As illustrated in Figure 3g,h, the qRT-PCR results show that, under the co-stimulation of HG and LPS, the transcription level of TXNIP and HDAC4 increases significantly. The TXNIP and HDAC4 decreased with the TSA pretreatment, indicating TSA's successful TXNIP and HDAC4 regulation. Furthermore, as the WB has shown in Figure 3k,l, TSA with a concentration of 16 ng mL⁻¹ has the most inhibited effect on the protein expression of TXNIP and HDAC4 in cell pyroptosis.

Macrophage phenotype is also crucial in inflammation. CD86 and CD206 are used as M1 and M2 macrophage indicators, respectively, to assess inflammation changes in diabetic wound cellular pyroptosis. The HG + LPS group has a relatively high CD86 level but a low CD206 level, revealing that the cells in the HG + LPS group are still in the inflammation process. With the administration of TSA pretreatment, compared to the HG + LPS group, TSA groups show a significant decrease in CD86 and increased CD206 expression, especially in the HG + TSA (16 ng mL⁻¹) + LPS group (Figure 3i–l). To further verify the effective macrophage phenotype transition after TSA pretreatment, the pro-inflammatory chemokines are measured by qRT-PCR and ELISA. As shown in Figure S3, both on the mRNA and protein level, the pro-inflammatory chemokines TNF- α and IL-6 are much lower in the HG + TSA (4 ng mL⁻¹) + LPS group and HG + TSA (16 ng mL⁻¹) + LPS group than in the HG + LPS group.

3.3. Design, Fabrication, and Characterization of MN-Mediated TSA Patch. To reduce the probability of injection-caused iatrogenic secondary damage for fragile diabetic wound and granulation tissue, with advantages of the microneedle (MN) minimally invasive way to pierce the skin barrier for drug administration and TSA inflammation regulation potential, we develop a swelling modified MN-mediated patch loaded with TSA for the subsequent experiments in vivo. The MN-mediated patch is fabricated via a micro-molding approach. Briefly, TSA powder and AlgMA are resuspended in dimethyl sulfoxide (DMSO) using vacuum

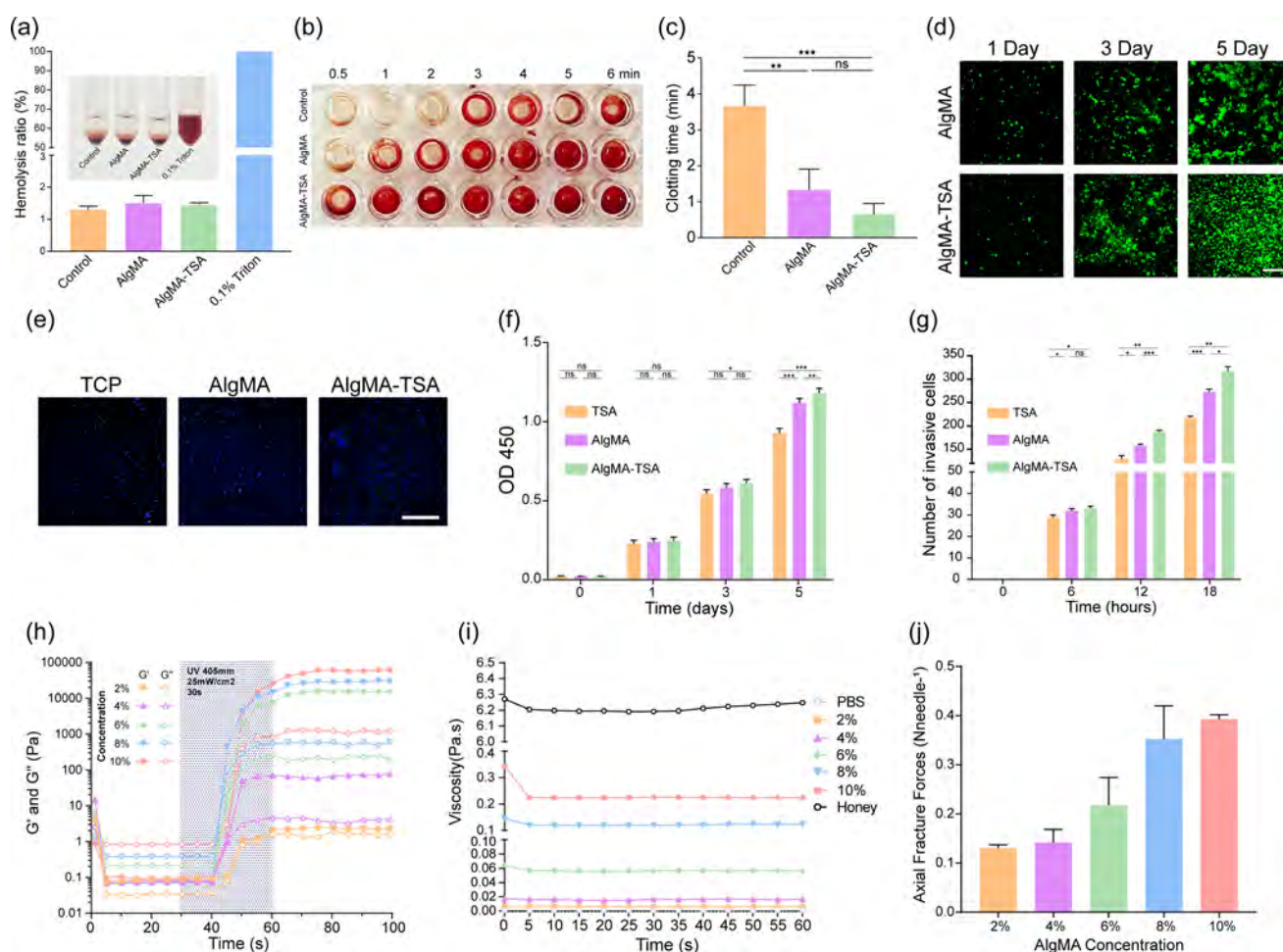


Figure 4. Cell biocompatibility, adhesion, proliferation, migration in vitro, and characterization of the MN-mediated TSA patch. (a) Hemolytic percentage of the control group, AlgMA group, AlgMA-TSA group, and positive control group. The HR value of these hydrogels is less than 2%, demonstrating that they are blood-compatible ($N = 3$). (b) Blood clot formation image in relation to time for the control group (no treatment), 8% AlgMA hydrogels (AlgMA group), and 8% AlgMA containing TSA hydrogels (AlgMA-TSA group). (c) Blood clotting time of each group ($N = 3$). (d) Live/dead staining of ECFCs after culture on 8% AlgMA hydrogels (AlgMA group) and 8% AlgMA containing TSA hydrogels (AlgMA-TSA group) for 1, 3, and 5 days. Scale bar is 200 μm . (e) Adherence of cells to the surface of TCP culture dishes (TCP control group), 8% AlgMA hydrogels (AlgMA group), and 8% AlgMA containing TSA hydrogels (AlgMA-TSA group). AlgMA-TSA groups can rapidly promote cell adhesion and disperse evenly. Scale bar is 200 μm . (f) Proliferation of ECFCs incubated for 0, 1, 3, and 5 days on TCP culture dishes with 16 ng mL^{-1} TSA (TSA control group), 8% AlgMA hydrogels (AlgMA group), and 8% AlgMA containing TSA hydrogels (AlgMA-TSA group) ($N = 3$). (g) The number of invasive ECFCs in the gap closure migration experiment with 16 ng mL^{-1} TSA (TSA control group), 8% AlgMA hydrogels (AlgMA group), and 8% AlgMA containing TSA hydrogels (AlgMA-TSA group). The number of cells that have invaded a central cell-free zone at the specified time points ($N = 3$) is used to quantify the migration of cells. (h) The energy storage and loss modulus of pre-gel before and after UV light. (i) The viscosity of AlgMA increases from 2 to 10% gradually. Honey and PBS are positive control and negative control groups, respectively. (j) Axial fracture forces of the MN-mediated TSA patch with different AlgMA concentrations. Data are represented as mean \pm SD ($N = 3$, each experiment is performed thrice). $*P < 0.05$, $**P < 0.01$, $***P < 0.001$.

impregnation methods and incubated in a 36 $^{\circ}\text{C}$ water bath until complete dissolution. After that, the pre-gel aqueous solution is cast into the mold, vacuumed for 20 min, and then solidified by UV light (Figure 5b). AlgMA is a modified sodium alginate added double bond that can be cross-linked and cured into homogeneity glue by UV light, which is highly portable compared with the traditional two-valence ion (calcium ions) cross-linking (Figure S4a). Proton nuclear magnetic resonance (PMR) shows successful conjugation, with the methacrylate peaks at 5.60 and 6.10 ppm (Figure S4b). In this study, TSA and AlgMA are bound together through electrostatic interactions (Figure S4c).

Before and after UV light, the pre-gel storage modulus (elastic modulus, G') and loss modulus (viscous modulus, G'') are analyzed. After UV light, G' of pre-gel is higher than the

G'' ; among them, the differences between the G' value and G'' value of 10, 8, and 6% are very remarkable (Figure 4h). The viscosity increases gradually, and the size of the pores is found to decrease, when the concentration of AlgMA increases from 2 to 10% (Figure 4i,j and Figure S5a–f). In comparison, the poor fluidity leads to the ineffectual formation of MNs under a concentration of 10% so is the pore size (another microneedle without TSA is prepared to observe the pore size clearly.) (Figure S5f). At the same time, AlgMA solutions with concentrations of 2, 4, and 6% cannot form microneedles effectively due to the lower mechanical strength caused by the low AlgMA content (Figure S6b–d). Notably, when the AlgMA concentration reaches 8%, the MNs can withstand compressive forces of more than 0.3 N per needle, which is sufficient for a successful skin puncture (Figure 4j and Figure

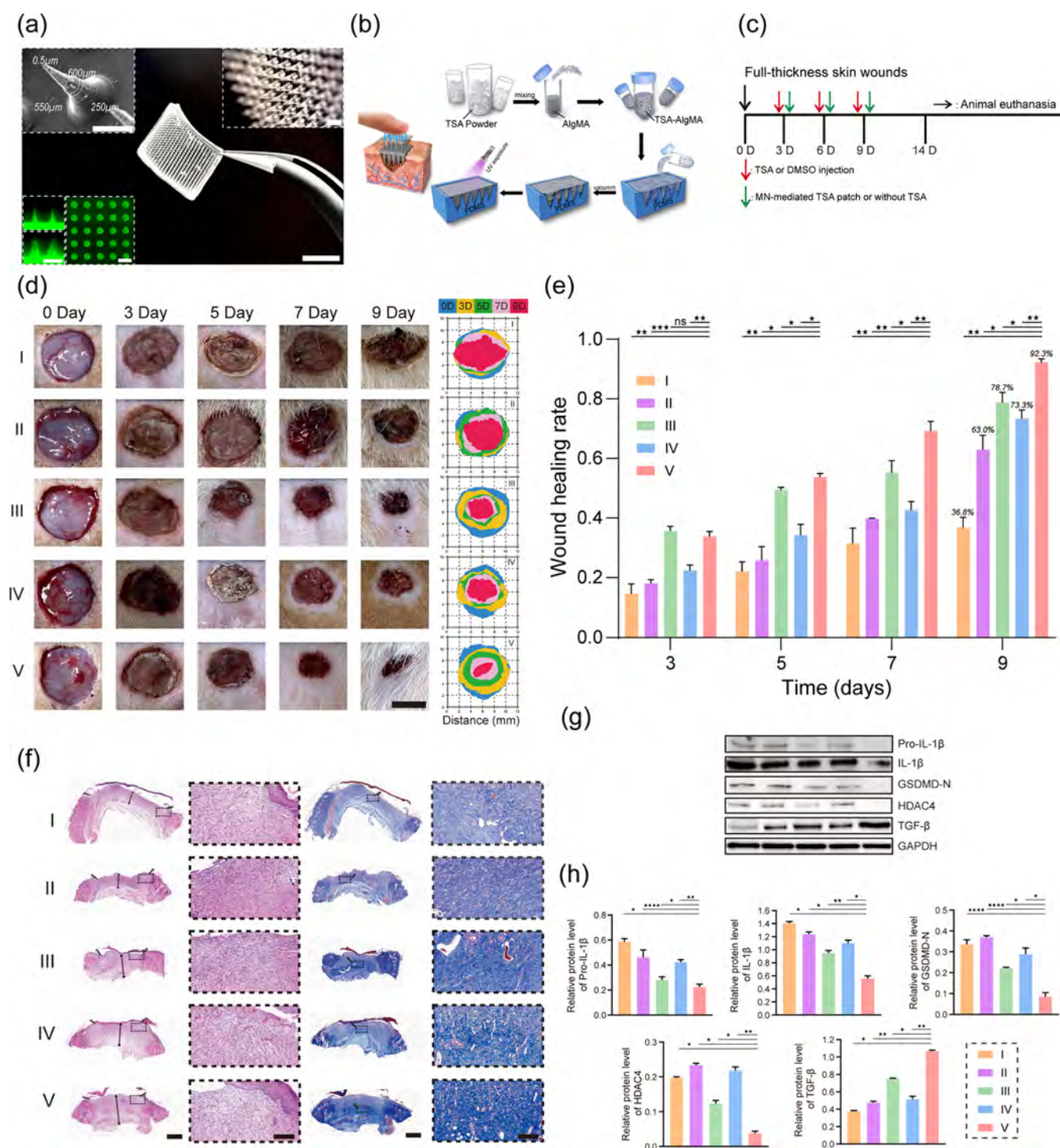


Figure 5. Evaluation of the MN-mediated TSA patch on wound healing of diabetic rats. (a) Optical, fluorescence, and SEM images of the microneedle. The top left shows the SEM image of the single needle, and every single needle possesses a conical shape with a tip diameter of 5 μm , a height of 600 μm , a base diameter of 250 μm , and a pin spacing of 550 μm ; scale bar is 200 μm ; the bottom left shows the fluorescence images of the microneedle before or after swelling 2 h with 36 $^{\circ}\text{C}$ PBS, scale bars are 200 μm , and the five rows of the microneedle array, scale bar is 550 μm ; the top right shows the optical image of the part of the microneedle (100 \times), scale bar is 0.5 mm; the median figure shows the optical image of the whole microneedle, scale bar is 1 cm. (b) Workflow for the fabrication of the microneedle arrays. (c) Timeline for the in vivo evaluation of various therapies. (d) Photographs and a graphic illustrating the wound's 9 day healing process following various treatments. It is shown that the MN-mediated TSA patch has the best therapeutic effect. Scale bar is 0.5 cm ($N = 3$). (e) Quantitative analysis of the relative diabetic wound area at different time points ($N = 3$). (f) H&E staining and Masson staining of the wound beds on day 9. Scale bars are 1 mm in 1 \times and 200 μm in 100 \times . H&E staining and Masson staining results indicated that TSA can significantly improve the thickness of granulation tissues and collagen deposition, especially in the MN-mediated TSA patch group. WB (g) and relative protein analyses (h) of Pro-IL-1 β , IL-1 β , GSDMD-N, and HDAC4 of diabetic wounds on day 9, which show that the inflammatory factors and diabetic wound hub gene protein levels are lower in the TSA treated groups, especially in the MN-mediated TSA patch treated group. The pro-healing factor TGF- β 1 protein level is highest in the MN-mediated TSA patch treated group followed by the TSA injection group. (I, II, III, IV, and V denote DM control, DMSO injection, TSA injection, MN-mediated

Figure 5. continued

patch without TSA, and MN-mediated TSA patch, respectively). Data are represented as mean \pm SD ($N = 3$, each experiment is performed thrice). * $P < 0.05$, ** $P < 0.01$, *** $P < 0.001$, **** $P < 0.0001$.

S6a). Therefore, an AlgMA concentration of 8% is adopted. As the swelling rate of the hydrogel is related to effusion fluids from the wound exudate and the alteration of the patch volume, the swelling rate of the 8% AlgMA hydrogel is characterized. As shown in Figure S5g, 8% AlgMA reaches the swelling ratio ($\approx 250\%$) in pre 30 min and swelling equilibrium ($\approx 590\%$) in 360 min. Because of the hydrophilic structure and high porosity of hydrogel, the 8% AlgMA MN-mediated patch can absorb effusion fluids and blood in the early stages quickly and then keep a moist healing environment while maintaining a stable shape and volume, avoiding continued compression to the diabetic wounds and surrounding fragile granulation tissue. Moreover, with the FITC-TSA as a demo, the drug in vitro release was carried out. The sustainable drug release capacity of the MN-mediated TSA patch is demonstrated via the Franz diffusion cell using a glutaraldehyde cross-linked gelatin film containing 80% water to simulate skin. As shown in Figure S5h, the total amount of FITC-TSA release in Alg-FITC-TSA microneedles is more than 40% within an hour, while the amount of FITC-TSA release in AlgMA-FITC-TSA patches is about 8% within an hour. After 24 h, the FITC-TSA release of Alg-FITC-TSA patches reaches 99% close to complete release, while when the AlgMA-FITC-TSA patches are still less than 75%, the complete release of AlgMA-FITC-TSA patches is nearly 72 h. The rapid drug release of Alg-FITC-TSA patches is due to the rapid dissolution of Alg. The slow FITC-TSA release behavior of AlgMA-FITC-TSA microneedles is due to the gradual swelling of the AlgMA cross-linked network.

Finally, the resulting MN-mediated TSA patch is arranged in 14.5 mm \times 14.5 mm containing 400 microneedles. Each microneedle possesses a conical shape with a tip diameter of 5 μ m, a height of 600 μ m, a base diameter of 250 μ m, and a pin spacing of 550 μ m. At the same time, the magnified microstructure can be further observed through SEM images. The fluorescence images show the microneedle before and after swelling for 2 h with PBS (Figure 5a).

3.4. Cell Biocompatibility, Adhesion, Proliferation, and Migration In Vitro. Tissue engineering requires cell-material interaction. Cell adhesion governs cell proliferation, migration, differentiation, and other critical cell functions.⁴⁸ Previous research has shown that TSA can promote migration of human endothelial colony forming cell (ECFC) paracrine function through the SDF-1/CXCR4 axis to enhance revascularization efficiency.⁴⁹ Due to cell adhesion, AlgMA has been widely used in wound healing.⁵⁰

It is necessary for hydrogels to have good biocompatibility before being used in therapeutic settings. A hemolysis assay is used to examine hydrogel blood compatibility; thus the hemolytic rate (HR) is an essential determinant of biomaterial compatibility.⁵¹ The HR values of 8% AlgMA hydrogels and 8% AlgMA containing TSA (TSA is 16 ng mL⁻¹ in hydrogels, according to the previous study: evaluation of TSA in vitro) are below 2%, demonstrating that these hydrogels are compatible with blood (Figure 4a). Meanwhile, the blood clotting effect of hydrogels shows that 8% AlgMA containing TSA hydrogels can promote blood clotting in 1 min, indicating that these hydrogels have good hemostatic properties (Figure 4b,c). Furthermore, the cytotoxicity of different hydrogels on

ECFCs is measured by the live/dead assay. After being cultured for 5 days, it is demonstrated that ECFCs are viable on 8% AlgMA hydrogels and 8% AlgMA containing TSA with over 80% viability (Figure 4d). According to the ISO 10993-5 standard, cells cultivated on the hydrogels do not exhibit any possible cytotoxicity on the same day.⁵² As seen in Figure 4e, after 6 h, ECFCs adhere to the 8% AlgMA containing TSA hydrogels efficiently, compared to the other groups. It is indicated that 8% AlgMA containing TSA hydrogels increase cell adherence and disperse uniformly very quickly. The CCK-8 assay is additionally used to quantify the proliferation of ECFCs grown with various treatments. After being incubated for 3 days, cells cultivated on the hydrogels exhibit good cell proliferation when compared to the TSA control group without hydrogels (TSA is 16 ng mL⁻¹ in DMSO). This is particularly true for the 8% AlgMA containing TSA hydrogel group. Moreover, the 8% AlgMA containing TSA hydrogel group is still better than other groups in the later time (Figure 4f). In the gap closure migration experiment, the 8% AlgMA containing TSA hydrogel group shows a significant increase in the cell invasive number, compared to the other groups with the time from 0 to 18 h (Figure 4g).

In this study, 8% AlgMA containing TSA hydrogel exhibits excellent hemostatic properties, cytocompatibility, and adhesion, superior proliferation and migration, and perfect blood compatibility compared to the 8% AlgMA hydrogel group. Overall, AlgMA and TSA can work together to give cells on hydrogels more adherent sites, creating a superior effect on cell adhesion, spreading, and proliferation.⁵⁰

3.5. Diabetic Wound Healing Study, Collagen Deposition, and Angiogenesis In Vivo. Five experimental groups (each group has six rats), i.e., diabetes mellitus (DM) control (non-treatment), DMSO injection (injection similar with TSA injection), TSA injection (7.5 mg mL⁻¹ TSA in DMSO, twice a week, 0.2 mL solution including 1.5 mg of TSA, per injection on days 0, 3, and 6; 4.5 mg of TSA per rat with 9 days), MN-mediated patch without TSA (treatment similar with the MN-mediated TSA patch), and MN-mediated TSA patch (1.5 mg of TSA per patch on days 0, 3, and 6; 4.5 mg of TSA per rat with 9 days), are categorized and conducted on rats with diabetic wounds modeled on the back (Figure 5c). Recording the wound healing process on days 0, 3, 5, 7, and 9 shows that the MN-mediated TSA patch has the best therapeutic effect (Figure 5d). Based on the quantitative analysis depicted in Figure 5e, the wound healing rate of the MN-mediated TSA patch group reaches nearly 93%, whereas the TSA injection group and MN-mediated patch without the TSA group still have 21.3 and 26.7% of regions unhealed, respectively.

Inflammatory wounds require regenerative regeneration, and the granulation tissue is essential to this process.⁵³ Therefore, a crucial sign for determining the repair impact of wound healing is a thicker granulation tissue. Hematoxylin and eosin (H&E) staining results demonstrate the regenerated granulation tissue at the wound bed on day 9, as shown in Figure 5f. The granulation tissue thicknesses in the experimental group of DM control, DMSO injection, TSA injection, MN-mediated patch without TSA, and MN-mediated TSA patch are 0.93, 1.09,

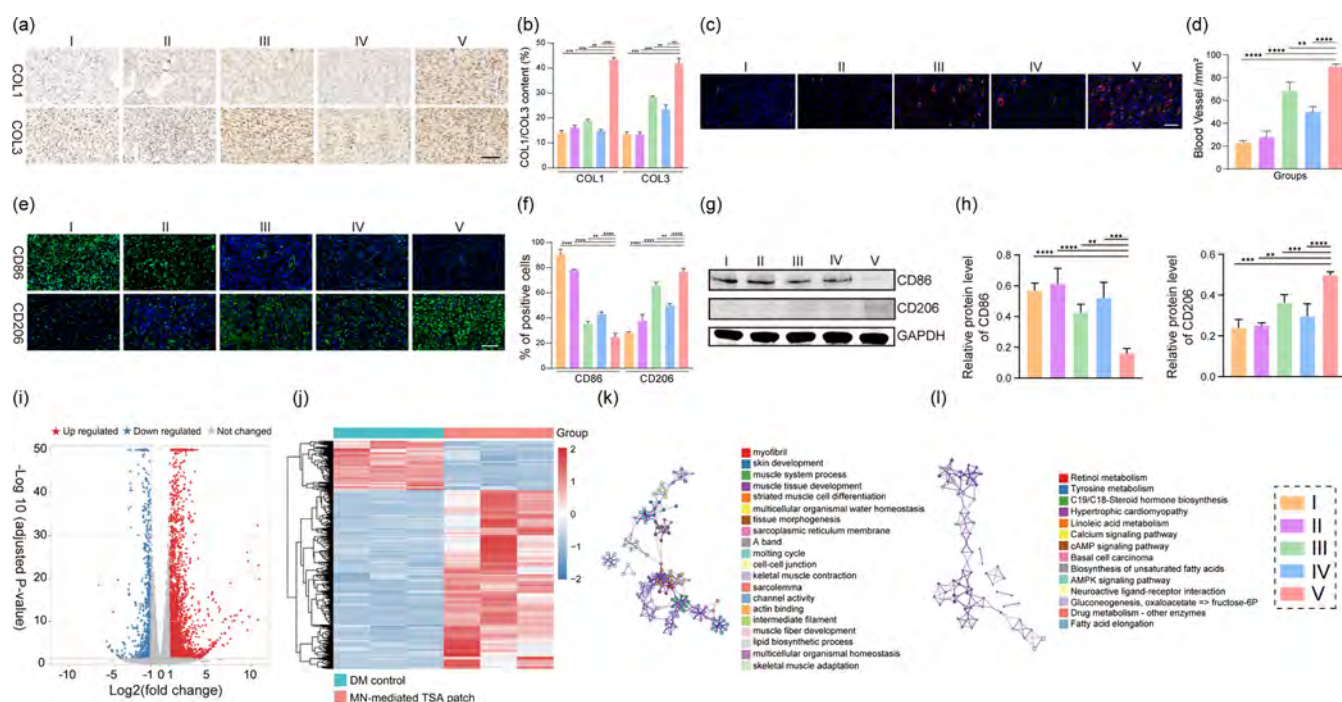


Figure 6. Collagen deposition, vascularization, macrophage phenotype, and RNA-seq analysis on wound healing of diabetic rats. (a) COL1 and COL3 immunohistochemical staining are used to assess the collagen deposition of diabetic wounds on day 9. (b) In wounds treated with the MN-mediated TSA patch, COL1 and COL3 expressions are highest, demonstrating that most mature collagen is generated in this group. Compared with the TSA injection group, the COL1 and COL3 densities of the MN-mediated TSA patch group are significantly increased ($N = 3$). Scale bar is $100\ \mu\text{m}$. (c) On day 9, there is a corresponding double immunofluorescence staining of CD31 and α -SMA. The vascular ducts are indicated by the arrows. Scale bar is $100\ \mu\text{m}$. (d) On day 9, a quantitative examination of blood vessel density ($N = 3$) is performed. The MN-mediated TSA patch group has more mature capillaries, as evidenced by the fact that wounds treated with this patch have the highest blood vessel density when compared to other groups. Corresponding double immunofluorescence staining of CD86 and CD206 (e) and quantitative analysis (f) in the wound tissues treated with different treatments on day 9. Scale bar is $100\ \mu\text{m}$. WB results (g) and relative protein level (h) of CD86 and CD206 in the wound tissues treated with different treatments on day 9. Volcano plot (i) and heatmap (j) of DEGs, including 4205 upregulated genes and 1036 downregulated genes ($|\log_2(\text{fold change})| \geq 1$ and $\text{adjust } P < 0.05$) in the MN-mediated TSA patch group. GO analysis (k) and KEGG analysis (l) between the DM control group and MN-mediated TSA patch group. Collectively, these high-throughput sequencing results demonstrate that the tissues under MN-mediated TSA patch treatment have better wound repairability. (I, II, III, IV, and V denote DM control, DMSO injection, TSA injection, MN-mediated patch without TSA, and MN-mediated TSA patch, respectively). Data are represented as mean \pm SD ($N = 3$, each experiment is performed thrice). ** $P < 0.01$, *** $P < 0.001$, **** $P < 0.0001$.

1.75, 1.71, and 2.25 mm, respectively. The granulation tissue of the non-TSA treatment groups is thinner than that of the TSA treatment groups. When compared to TSA injection, the granulation tissue formed by the MN-mediated TSA patch has a thicker tendency, indicating that the MN-mediated TSA patch has the best wound repair effect. Vascularization and collagen deposition are also essential for enhancing the creation of the ECM formation.⁵⁴ After 9 days, the MN-mediated TSA patch has the highest collagen fiber density in the wound bed, compared to the other groups, according to the results of Masson's trichrome staining. It appears that the MN-mediated TSA patch group exhibits noticeably increased ECM deposition (Figure 5f). Additionally, after 9 days, COL1 and COL3 immunohistochemical staining are used to evaluate the collagen deposition of diabetic wounds.⁵⁵ Figure 6a shows that wounds treated with MN-mediated TSA patches express the most expression of COL1 and COL3, indicating that the most mature collagen is formed in this group (Figure 6b). In addition, after 9 days of treatment, α -SMA (a marker of the vascular smooth muscle cells) and CD31 (a vascular endothelial cell marker) immunofluorescence staining are used to evaluate the angiogenesis of each group. Figure 6c demonstrates that the expression of α -SMA and CD31 is highest in wounds treated with the MN-mediated TSA patch,

indicating that the MN-mediated TSA patch group forms the majority of mature capillaries (Figure 6d). Thus, the MN-mediated TSA patch is conducive to vascular endothelial adherence and proliferation, promoting angiogenesis. In line with these findings, the MN-mediated TSA patch greatly increases the expression of the pro-healing factor transforming growth factor beta-1 (TGF- β 1) in the wound tissues (Figure 5g,h).

3.6. Inflammation, RNA Sequencing, and Toxicity In Vivo

Inflammation starts the complete healing cascade throughout the diabetic wound healing process, which is important to the healing outcome. HDAC4 is used as the hub gene of diabetic wounds, and Pro-IL-1 β , IL-1 β , and GSDMD-N are used as indicators of pyroptosis to evaluate the level of inflammation in groups following various therapies. On day 9, TSA treatment groups show a good degree of inflammation control. Among the five groups, the Pro-IL-1 β , IL-1 β , GSDMD-N, and HDAC4 in the MN-mediated TSA patch group are the lowest (Figure 5g,h). What is more, the M2 macrophage (CD206) in the MN-mediated TSA patch group is the highest and the M1 macrophage (CD86) in the MN-mediated TSA patch group is the lowest among the five groups (Figure 6e–h). Above all, the diabetic wounds in the TSA treatment groups (especially in the MN-mediated TSA patch

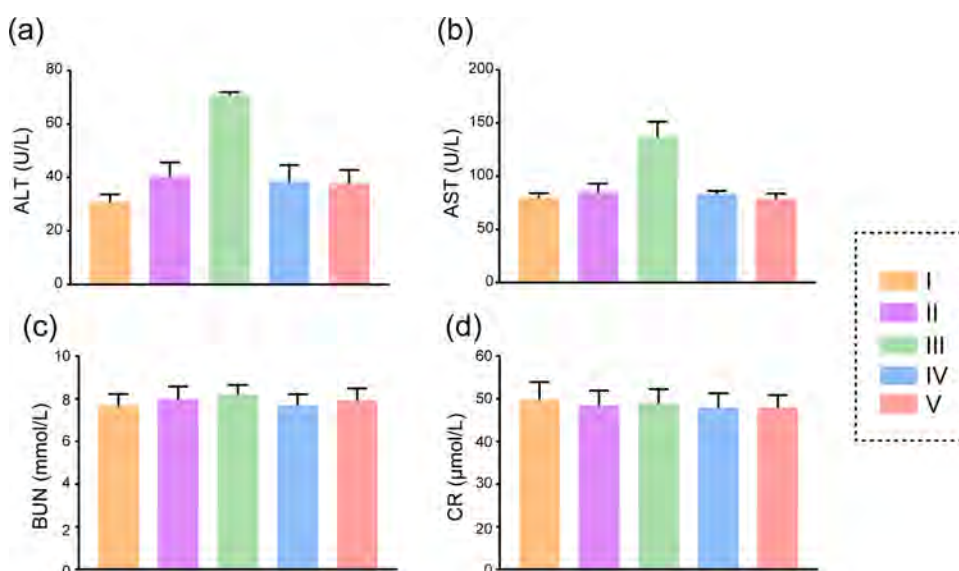


Figure 7. Biochemical factors of animals with different treatments. (a) Alanine amino transferase (ALT) level in different treatment groups. (b) Aspartate amino transferase (AST) level in rats with different treatments. (c) Blood urea nitrogen (BUN) level in different treatment groups. (d) Different treatments affect the creatinine (CR) level in rats. On day 10, the biochemical parameters of blood from the rat at 24 h after the last various treatment are evaluated for different treatments in the rat. The liver and kidney function parameters are within the normal range in the MN-mediated TSA patch group. Compared with other groups, relatively high levels of ALT and AST are induced in the TSA injection group, indicating that the TSA injection induced hepatic dysfunction ($N = 3$). (I, II, III, IV, and V denote DM control, DMSO injection, TSA injection, MN-mediated patch without TSA, and MN-mediated TSA patch, respectively). Data are represented as mean \pm SD ($N = 3$, each experiment is performed thrice).

group) have passed the inflammatory stage on day 9 and can transition to the next stage of healing, but the non-TSA treatment groups are still in the inflammatory phase.

RNA sequencing is utilized and performed on DEGs of DM rats, including three DM rats in the MN-mediated TSA patch group and three DM rats in the control group, to evaluate the wound healing conditions, such as cytokines, epigenetic regulation, and so on. Compared with the control group, the DM rats in the MN-mediated TSA patch group have 4205 upregulated mRNAs and 1036 downregulated genes ($|\log_2(\text{fold change})| \geq 1$ and adjust $P < 0.05$), as shown in Figure 6i,j. From the GO analysis shown in Figure 6k and Figure S7a, it is observed that DEGs are predominantly associated with tissue remodeling, e.g., myofibril (GO:0030016), skin development (GO:0043588), muscle system process (GO:0003012), muscle tissue development (GO:0060537), and striated muscle cell differentiation (GO:0051146). Regarding the KEGG pathway, the results depicted in Figure 6l and Figure S7b demonstrate that DEGs are significantly associated with wound regeneration and repair, e.g., retinol metabolism (ko00830) and tyrosine metabolism (ko00350). Collectively, these high-throughput sequencing results demonstrate that the tissues under MN-mediated TSA patch treatment have better wound reparability.

To confirm the safety profile of the MN-mediated TSA patch, we last evaluate the in vivo toxicity. The blood biochemical parameters on day 10 (biochemical parameters of blood from the rat at 24 h after the last various treatments) are evaluated for different treatments in the rat (Figure 7). The MN-mediated TSA patch group's functional metrics for the liver and kidneys are within the normal range. However, the TSA injection group exhibits relatively high levels of alanine amino transferase (ALT) and aspartate amino transferase (AST) (Figure 7a,b), suggesting that the TSA injection causes hepatic dysfunction.

4. CONCLUSIONS

Diabetes mellitus and related secondary complications affect and threaten the lives of 440 million people worldwide, among which diabetic wounds (such as diabetic foot ulcers) are one of the most severe complications and hard to heal.⁵⁶ However, specific medicine and treatment for effective diabetic wound healing are still lacking. Here, with the guidance of AI-assisted bioinformatics, therapeutic mechanisms, genes, and drugs are found, which dramatically promote the precise treatment in diabetic wounds and reduce the research resources and cost. We design, fabricate, and explore an MN-mediated TSA patch that simultaneously regulates inflammation, tissue regeneration, and hub gene to promote diabetic wound healing in a low-invasive transdermal manner. Additionally, the micro-structure of MNs allows for efficient medication delivery to the target location while minimizing skin and patch adherence. Compared to the traditional injection treatment that may cause iatrogenic damage in diabetic wound healing, our MN-mediated TSA patch is a low toxicity, gentle, and long-lasting transdermal drug delivery system that can promote the diabetic wound healing via regulating inflammation, hub gene, and tissue regeneration. Furthermore, the integration of AI-assisted bioinformatics analysis, the new application of old drugs, and polymeric materials provide a brand new research direction for chronic wounds and will find tremendous potential for promoting wound healing and broad medical treatments.

■ ASSOCIATED CONTENT

Supporting Information

The Supporting Information is available free of charge at <https://pubs.acs.org/doi/10.1021/acsami.2c08994>.

Figure S1. Enriched terms visualized in the bubble plot of DEGs of GSE144441; Figure S2. TSA and glucose concentration selection in vitro; Figure S3. TNF- α and

IL-6 measured by qRT-PCR and ELISA in vitro; Figure S4. PMR spectra and electrostatic interaction; Figure S5. Fabrication and characterization of AlgMA hydrogels; Figure S6. Schematic illustration of the mechanical strength test process and the characterization information of unformed microneedles; Figure S7. RNA-sequencing support information on wound healing of diabetic rats; Table S1. Information of the 10 prospective drugs with significant scores for diabetic wound treatment; Table S2. List of qRT-PCR primers used in the current study; Table S3. Random blood glucose concentration before and after STZ injection (mmol L^{-1}); Table S4. Body weight of diabetic and control rats before and after STZ injection (mmol L^{-1}); Table S5. Antibodies used in the current study (PDF)

AUTHOR INFORMATION

Corresponding Authors

Haojian Lu — State Key Laboratory of Industrial Control and Technology and Institute of Cyber-Systems and Control, the Department of Control Science and Engineering, Zhejiang University, Hangzhou 310027, China; orcid.org/0000-0002-1393-3040; Email: luhaojian@zju.edu.cn

Weiqliang Tan — Department of Plastic Surgery, Sir Run Run Shaw Hospital, Zhejiang University of Medicine, Hangzhou 310016, China; Email: tanweiqlxxx@zju.edu.cn

Authors

Yanan Xue — State Key Laboratory of Industrial Control and Technology and Institute of Cyber-Systems and Control, the Department of Control Science and Engineering, Zhejiang University, Hangzhou 310027, China; Department of Plastic Surgery, Sir Run Run Shaw Hospital, Zhejiang University of Medicine, Hangzhou 310016, China; orcid.org/0000-0002-8406-6263

Cheng Chen — Stomatology Hospital, School of Stomatology, Zhejiang University School of Medicine, Zhejiang Provincial Clinical Research Center for Oral Diseases, Key Laboratory of Oral Biomedical Research of Zhejiang Province, Cancer Center of Zhejiang University, Hangzhou 310000, China; orcid.org/0000-0001-9870-5890

Rong Tan — Department of Biomedical Engineering, City University of Hong Kong, Hong Kong 999077, China; orcid.org/0000-0002-3207-7817

Jingyu Zhang — State Key Laboratory of Industrial Control and Technology and Institute of Cyber-Systems and Control, the Department of Control Science and Engineering, Zhejiang University, Hangzhou 310027, China

Qin Fang — State Key Laboratory of Industrial Control and Technology and Institute of Cyber-Systems and Control, the Department of Control Science and Engineering, Zhejiang University, Hangzhou 310027, China

Rui Jin — State Key Laboratory of Industrial Control and Technology and Institute of Cyber-Systems and Control, the Department of Control Science and Engineering, Zhejiang University, Hangzhou 310027, China

Xiangyu Mi — State Key Laboratory of Industrial Control and Technology and Institute of Cyber-Systems and Control, the Department of Control Science and Engineering, Zhejiang University, Hangzhou 310027, China

Danying Sun — State Key Laboratory of Industrial Control and Technology and Institute of Cyber-Systems and Control,

the Department of Control Science and Engineering, Zhejiang University, Hangzhou 310027, China

Yinan Xue — College of Biotechnology and Bioengineering, Zhejiang University of Technology, Hangzhou 310014, China; orcid.org/0000-0003-0214-5513

Yue Wang — State Key Laboratory of Industrial Control and Technology and Institute of Cyber-Systems and Control, the Department of Control Science and Engineering, Zhejiang University, Hangzhou 310027, China

Rong Xiong — State Key Laboratory of Industrial Control and Technology and Institute of Cyber-Systems and Control, the Department of Control Science and Engineering, Zhejiang University, Hangzhou 310027, China

Complete contact information is available at:

<https://pubs.acs.org/10.1021/acsami.2c08994>

Author Contributions

[▽]Y.X. and C.C. equally contributed to this work. All of the authors contributed to the writing of the manuscript. The final version of the manuscript has been approved by every author.

Funding

This work was supported by the National Science Foundation of China (62173293), the Fundamental Research Funds for the Zhejiang Provincial Universities (2021XZZX021), Zhejiang Provincial Natural Science Foundation of China (LD22E050007), and the Key R&D Program of Zhejiang (2022C01022).

Notes

The authors declare no competing financial interest.

REFERENCES

- (1) Brody, H. Diabetes. *Nature* **2012**, 485, S1.
- (2) Grennan, D. Diabetic Foot Ulcers. *Jama* **2019**, 321, 114.
- (3) Wang, J.; Wu, H.; Peng, Y.; Zhao, Y.; Qin, Y.; Zhang, Y.; Xiao, Z. Hypoxia Adipose Stem Cell-Derived Exosomes Promote High-Quality Healing of Diabetic Wound Involves Activation of PI3K/Akt Pathways. *J. Nanobiotechnology* **2021**, 19, 202.
- (4) Xu, Z.; Liang, B.; Tian, J.; Wu, J. Anti-Inflammation Biomaterial Platforms for Chronic Wound Healing. *Biomater. Sci.* **2021**, 9, 4388–4409.
- (5) Fiona Louis, M. P.; Liu, H.; Kang, D.-H.; Sowa, Y.; Kitano, S.; Matsusaki, M. Bioprinted Vascularized Mature Adipose Tissue with Collagen Microfibers for Soft Tissue Regeneration. *Cyborg Bionic Syst.* **2021**, 2021, 15.
- (6) Zhao, R.; Liang, H.; Clarke, E.; Jackson, C.; Xue, M. Inflammation in Chronic Wounds. *Int. J. Mol. Sci.* **2016**, 17, 2085.
- (7) Wang, Y.; Gao, W.; Shi, X.; Ding, J.; Liu, W.; He, H.; Wang, K.; Shao, F. Chemotherapy Drugs Induce Pyroptosis Through Caspase-3 Cleavage of A Gasdermin. *Nature* **2017**, 547, 99–103.
- (8) Zhou, R.; Yazdi, A. S.; Menu, P.; Tschoopp, J. A Role for Mitochondria in NLRP3 Inflammasome Activation. *Nature* **2011**, 469, 221–225.
- (9) Liu, D.; Yang, P.; Gao, M.; Yu, T.; Shi, Y.; Zhang, M.; Yao, M.; Liu, Y.; Zhang, X. NLRP3 Activation Induced by Neutrophil Extracellular Traps Sustains Inflammatory Response in the Diabetic Wound. *Clin. Sci.* **2019**, 133, 565–582.
- (10) Bergsbaken, T.; Fink, S. L.; Cookson, B. T. Pyroptosis: Host Cell Death and Inflammation. *Nat. Rev. Microbiol.* **2009**, 7, 99–109.
- (11) Louiselle, A. E.; Niemiec, S. M.; Zgheib, C.; Liechty, K. W. Macrophage Polarization and Diabetic Wound Healing. *Transl. Res.* **2021**, 236, 109–116.
- (12) Ganesh, G. V.; Ramkumar, K. M. Macrophage Mediation in Normal and Diabetic Wound Healing Responses. *Inflammation Res.* **2020**, 69, 347–363.

- (13) Rehman, K.; Akash, M. S. Mechanisms of Inflammatory Responses and Development of Insulin Resistance: How are They Interlinked? *J. Biomed. Sci.* **2016**, *23*, 87.
- (14) Alkhatatbeh, M. J.; Abdalqader, N. A.; Alqudah, M. A. Y. Impaired Awareness of Hypoglycaemia in Insulin-Treated Type 2 Diabetes Mellitus. *Curr. Diabetes Rev.* **2019**, *15*, 407–413.
- (15) Ansari, A. M.; Osmani, L.; Matsangos, A. E.; Li, Q. K. Current Insight in the Localized Insulin-Derived Amyloidosis (LIDA): Clinico-Pathological Characteristics and Differential Diagnosis. *Pathol. Res. Pract.* **2017**, *213*, 1237–1241.
- (16) Singha, A.; Bhattacharjee, R.; Dalal, B. S.; Biswas, D.; Choudhuri, S.; Chowdhury, S. Associations of Insulin-Induced Lipodystrophy in Children, Adolescents, and Young Adults with Type 1 Diabetes Mellitus Using Recombinant Human Insulin: A Cross-Sectional Study. *J. Pediatr. Endocrinol. Metab.* **2021**, *34*, 503–508.
- (17) Lamb, J.; Crawford, E. D.; Peck, D.; Modell, J. W.; Blat, I. C.; Wrobel, M. J.; Lerner, J.; Brunet, J. P.; Subramanian, A.; Ross, K. N.; Reich, M.; Hieronymus, H.; Wei, G.; Armstrong, S. A.; Haggarty, S. J.; Clemons, P. A.; Wei, R.; Carr, S. A.; Lander, E. S.; Golub, T. R. The Connectivity Map: Using Gene-Expression Signatures to Connect Small Molecules, Genes, and Disease. *Science* **2006**, *313*, 1929–1935.
- (18) Xue, J.; Zhang, B.; Dou, S.; Zhou, Q.; Ding, M.; Zhou, M.; Wang, H.; Dong, Y.; Li, D.; Xie, L. Revealing the Angiopathy of Lacrimal Gland Lesion in Type 2 Diabetes. *Front. Physiol.* **2021**, *12*, No. 731234.
- (19) Li, H.; Shi, X.; Jiang, H.; Kang, J.; Yu, M.; Li, Q.; Yu, K.; Chen, Z.; Pan, H.; Chen, W. CMap Analysis Identifies Atractyloside as A Potential Drug Candidate for Type 2 Diabetes Based on Integration of Metabolomics and Transcriptomics. *J. Cell Mol. Med.* **2020**, *24*, 7417–7426.
- (20) Bolden, J. E.; Peart, M. J.; Johnstone, R. W. Anticancer Activities of Histone Deacetylase Inhibitors. *Nat. Rev. Drug Discovery* **2006**, *5*, 769–784.
- (21) Karnam, K.; Sedmaki, K.; Sharma, P.; Routholla, G.; Goli, S.; Ghosh, B.; Venuganti, V. V. K.; Kulkarni, O. P. HDAC6 Inhibitor Accelerates Wound Healing by Inhibiting Tubulin Mediated IL-1 β Secretion in Diabetic Mice. *Biochim. Biophys. Acta, Mol. Basis Dis.* **2020**, *2020*, No. 165903.
- (22) Xu, S.; Chen, H.; Ni, H.; Dai, Q. Targeting HDAC6 Attenuates Nicotine-Induced Macrophage Pyroptosis via NF- κ B/NLRP3 Pathway. *Atherosclerosis* **2021**, *317*, 1–9.
- (23) Chen, X.; Barozzi, I.; Termanini, A.; Prosperini, E.; Recchiuti, A.; Dalli, J.; Mietton, F.; Matteoli, G.; Hiebert, S.; Natoli, G. Requirement for the Histone Deacetylase HDAC3 for the Inflammatory Gene Expression Program in Macrophages. *Proc. Natl. Acad. Sci. U. S. A.* **2012**, *109*, E2865–E2874.
- (24) Yao, F.; Jin, Z.; Zheng, Z.; Lv, X.; Ren, L.; Yang, J.; Chen, D.; Wang, B.; Yang, W.; Chen, L.; Wang, W.; Gu, J.; Lin, R. HDAC11 Promotes both NLRP3/Caspase-1/GSDMD and Caspase-3/GSDME Pathways Causing Pyroptosis via ERG in Vascular Endothelial Cells. *Cell Death Discovery* **2022**, *8*, 112.
- (25) Zhang, X.; Chen, G.; Liu, Y.; Sun, L.; Sun, L.; Zhao, Y. Black Phosphorus-Loaded Separable Microneedles as Responsive Oxygen Delivery Carriers for Wound Healing. *ACS Nano* **2020**, *14*, 5901–5908.
- (26) Yin, M.; Wu, J.; Deng, M.; Wang, P.; Ji, G.; Wang, M.; Zhou, C.; Blum, N. T.; Zhang, W.; Shi, H.; Jia, N.; Wang, X.; Huang, P. Multifunctional Magnesium Organic Framework-Based Microneedle Patch for Accelerating Diabetic Wound Healing. *ACS Nano* **2021**, *15*, 17842.
- (27) Yao, S.; Wang, Y.; Chi, J.; Yu, Y.; Zhao, Y.; Luo, Y.; Wang, Y. Porous MOF Microneedle Array Patch with Photothermal Responsive Nitric Oxide Delivery for Wound Healing. *Adv. Sci.* **2022**, *9*, No. e2103449.
- (28) Yuan, M.; Liu, K.; Jiang, T.; Li, S.; Chen, J.; Wu, Z.; Li, W.; Tan, R.; Wei, W.; Yang, X.; Dai, H.; Chen, Z. GelMA/PEGDA Microneedles Patch Loaded with HUVECs-Derived Exosomes and Tazarotene Promote Diabetic Wound Healing. *J. Nanobiotechnology* **2022**, *20*, 147.
- (29) Jinhua, Li, L. D.; Khezri, B.; Bing, W.; Zhou, H.; Sofer, Z. Biohybrid Micro- and Nanorobots for Intelligent Drug Delivery. *Cyborg Bionic Syst.* **2022**, *2022*, 13.
- (30) Yu, J.; Wang, J.; Zhang, Y.; Chen, G.; Mao, W.; Ye, Y.; Kahkoska, A. R.; Buse, J. B.; Langer, R.; Gu, Z. Glucose-Responsive Insulin Patch for the Regulation of Blood Glucose in Mice and Minipigs. *Nat. Biomed. Eng.* **2020**, *4*, 499–506.
- (31) Sheng, T.; Luo, B.; Zhang, W.; Ge, X.; Yu, J.; Zhang, Y.; Gu, Z. Microneedle-Mediated Vaccination: Innovation and Translation. *Adv. Drug Delivery Rev.* **2021**, *179*, No. 113919.
- (32) Vigushin, D. M.; Ali, S.; Pace, P. E.; Mirsaidi, N.; Ito, K.; Adcock, I.; Coombes, R. C. Trichostatin A is A Histone Deacetylase Inhibitor with Potent Antitumor Activity Against Breast Cancer in Vivo. *Clin. Cancer Res.* **2001**, *7*, 971–976.
- (33) Spallotta, F.; Cencioni, C.; Straino, S.; Nanni, S.; Rosati, J.; Artuso, S.; Manni, I.; Colussi, C.; Piaggio, G.; Martelli, F.; Valente, S.; Mai, A.; Capogrossi, M. C.; Farsetti, A.; Gaetano, C. A Nitric oxide-Dependent Cross-Talk between Class I and III Histone Deacetylases Accelerates Skin Repair. *J. Biol. Chem.* **2013**, *288*, 11004–11012.
- (34) Gao, Y.; Jin, X. Dual Crosslinked Methacrylated Alginate Hydrogel Micron Fibers and Tissue Constructs for Cell Biology. *Mar. Drugs* **2019**, *17*, 557.
- (35) Barrett, T.; Wilhite, S. E.; Ledoux, P.; Evangelista, C.; Kim, I. F.; Tomashevsky, M.; Marshall, K. A.; Phillippy, K. H.; Sherman, P. M.; Holko, M.; Yefanov, A.; Lee, H.; Zhang, N.; Robertson, C. L.; Serova, N.; Davis, S.; Soboleva, A. NCBI GEO: Archive for Functional Genomics Data Sets—Update. *Nucleic Acids Res.* **2012**, *41*, D991–D995.
- (36) Zhou, Y.; Zhou, B.; Pache, L.; Chang, M.; Khodabakhshi, A. H.; Tanaseichuk, O.; Benner, C.; Chanda, S. K. Metascape Provides A Biologist-Oriented Resource for the Analysis of Systems-Level Datasets. *Nat. Commun.* **2019**, *10*, 1523.
- (37) Szklarczyk, D.; Gable, A. L.; Nastou, K. C.; Lyon, D.; Kirsch, R.; Pyysalo, S.; Doncheva, N. T.; Legeay, M.; Fang, T.; Bork, P.; Jensen, L. J.; von Mering, C. The STRING Database in 2021: Customizable Protein-Protein Networks, and Functional Characterization of User-Uploaded Gene/Measurement Sets. *Nucleic Acids Res.* **2021**, *49*, D605–d612.
- (38) Chin, C. H.; Chen, S. H.; Wu, H. H.; Ho, C. W.; Ko, M. T.; Lin, C. Y. CytoHubba: Identifying Hub Objects and Sub-Networks from Complex Interactome. *BMC Syst. Biol.* **2014**, *8*, S11.
- (39) Shannon, P.; Markiel, A.; Ozier, O.; Baliga, N. S.; Wang, J. T.; Ramage, D.; Amin, N.; Schwikowski, B.; Ideker, T. Cytoscape: A Software Environment for Integrated Models of Biomolecular Interaction Networks. *Genome Res.* **2003**, *13*, 2498–2504.
- (40) Eberhardt, J.; Santos-Martins, D.; Tillack, A. F.; Forli, S. AutoDock Vina 1.2.0: New Docking Methods, Expanded Force Field, and Python Bindings. *J. Chem. Inf. Model.* **2021**, *61*, 3891–3898.
- (41) Bu, D.; Luo, H.; Huo, P.; Wang, Z.; Zhang, S.; He, Z.; Wu, Y.; Zhao, L.; Liu, J.; Guo, J.; Fang, S.; Cao, W.; Yi, L.; Zhao, Y.; Kong, L. KOBAS-i: Intelligent Prioritization and Exploratory Visualization of Biological Functions for Gene Enrichment Analysis. *Nucleic Acids Res.* **2021**, *49*, W317–w325.
- (42) Ai, C.; Kong, L. CGPS: A Machine Learning-Based Approach Integrating Multiple Gene Set Analysis Tools for Better Prioritization of Biologically Relevant Pathways. *J. Genet. Genomics* **2018**, *45*, 489–504.
- (43) Cabanel, M.; da Costa, T. P.; El-Cheikh, M. C.; Carneiro, K. The Epigenome as A Putative Target for Skin Repair: The HDAC Inhibitor Trichostatin A Modulates Myeloid Progenitor Plasticity and Behavior and Improves Wound Healing. *J. Transl. Med.* **2019**, *17*, 247.
- (44) Qiu, Z.; He, Y.; Ming, H.; Lei, S.; Leng, Y.; Xia, Z. Y. Lipopolysaccharide (LPS) Aggravates High Glucose and Hypoxia/Reoxygenation-Induced Injury through Activating ROS-Dependent NLRP3 Inflammasome-Mediated Pyroptosis in H9C2 Cardiomyocytes. *J. Diabetes Res.* **2019**, *2019*, 8151836.

- (45) Burdette, B. E.; Esparza, A. N.; Zhu, H.; Wang, S. Gasdermin D in Pyroptosis. *Acta Pharm. Sin., B* **2021**, *11*, 2768–2782.
- (46) Iyer, S. S.; He, Q.; Janczy, J. R.; Elliott, E. I.; Zhong, Z.; Olivier, A. K.; Sadler, J. J.; Knepper-Adrian, V.; Han, R.; Qiao, L.; Eisenbarth, S. C.; Nauseef, W. M.; Cassel, S. L.; Sutterwala, F. S. Mitochondrial Cardiolipin is Required for Nlrp3 Inflammasome Activation. *Immunity* **2013**, *39*, 311–323.
- (47) Zhou, R.; Tardivel, A.; Thorens, B.; Choi, I.; Tschopp, J. Thioredoxin-Interacting Protein Links Oxidative Stress to Inflammasome Activation. *Nat. Immunol.* **2010**, *11*, 136–140.
- (48) Subramaniam, T.; Fauzi, M. B.; Lokanathan, Y.; Law, The Role of Calcium in Wound Healing. *Int. J. Mol. Sci.* **2021**, *22*, 6486.
- (49) Palii, C. G.; Vulesevic, B.; Fraigneau, S.; Pranckeviciene, E.; Griffith, A. J.; Chu, A.; Faralli, H.; Li, Y.; McNeill, B.; Sun, J.; Perkins, T. J.; Dilworth, F. J.; Perez-Iratxeta, C.; Suuronen, E. J.; Allan, D. S.; Brand, M. Trichostatin A Enhances Vascular Repair by Injected Human Endothelial Progenitors through Increasing the Expression of TALL-Dependent Genes. *Cell Stem Cell* **2014**, *14*, 644–657.
- (50) Tavaafoghi, M.; Sheikhi, A.; Tutar, R.; Jahangiry, J.; Baidya, A.; Haghniaz, R.; Khademhosseini, A. Engineering Tough, Injectable, Naturally Derived, Bioadhesive Composite Hydrogels. *Adv. Healthcare Mater.* **2020**, *9*, No. e1901722.
- (51) Aggarwal, D.; Kumar, V.; Sharma, S. Drug-Loaded Biomaterials for Orthopedic Applications: A Review. *J. Controlled Release* **2022**, *344*, 113–133.
- (52) Fiocco, L.; Li, S.; Stevens, M. M.; Bernardo, E.; Jones, J. R. Biocompatibility and Bioactivity of Porous Polymer-Derived Ca-Mg Silicate Ceramics. *Acta Biomater.* **2017**, *50*, 56–67.
- (53) Schirmer, L.; Atallah, P.; Freudenberg, U.; Werner, C. Chemokine-Capturing Wound Contact Layer Rescues Dermal Healing. *Adv. Sci.* **2021**, *8*, No. e2100293.
- (54) Patel, S.; Srivastava, S.; Singh, M. R.; Singh, D. Mechanistic Insight into Diabetic Wounds: Pathogenesis, Molecular Targets and Treatment Strategies to Pace Wound Healing. *Biomed. Pharmacother.* **2019**, *112*, No. 108615.
- (55) Chen, E.; Yang, L.; Ye, C.; Zhang, W.; Ran, J.; Xue, D.; Wang, Z.; Pan, Z.; Hu, Q. An Asymmetric Chitosan Scaffold for Tendon Tissue Engineering: In Vitro and in Vivo Evaluation with Rat Tendon Stem/Progenitor Cells. *Acta Biomater.* **2018**, *73*, 377–387.
- (56) Worldwide Trends in Diabetes Since 1980: A Pooled Analysis of 751 Population-Based Studies with 4.4 Million Participants. *Lancet* **2016**, *387*, 1513–1530, DOI: 10.1016/S0140-6736(16)00618-8.

Recommended by ACS

Synthesis and Biological Screening of New 2-(5-Aryl-1-phenyl-1H-pyrazol-3-yl)-4-aryl Thiazole Derivatives as Potential Antimicrobial Agents

Yogesh Nandurkar, Pravin Chimaji Mhaske, *et al.*

FEBRUARY 22, 2023

ACS OMEGA

READ 

Evaluation of Broad Anti-Coronavirus Activity of Autophagy-Related Compounds Using Human Airway Organoids

Rina Hashimoto, Kazuo Takayama, *et al.*

MARCH 22, 2023

MOLECULAR PHARMACEUTICS

READ 

Fabrication and Properties of Biodegradable Akermanite-Reinforced Fe35Mn Alloys for Temporary Orthopedic Implant Applications

Meili Zhang, Matthew S. Dargusch, *et al.*

FEBRUARY 21, 2023

ACS BIOMATERIALS SCIENCE & ENGINEERING

READ 

Poly(l-lactic acid) Scaffold Releasing an $\alpha_4\beta_1$ Integrin Agonist Promotes Nonfibrotic Skin Wound Healing in Diabetic Mice

Vito Antonio Baldassarro, Laura Calzà, *et al.*

DECEMBER 21, 2022

ACS APPLIED BIO MATERIALS

READ 

Get More Suggestions >